



Fabrication and characterization of $\text{Pb}(\text{Zr}_{0.5}\text{Ti}_{0.5})\text{O}_3$ nanofibers for nanogenerator applications

Khizar Hayat¹ · Syed Shaheen Shah² · Shahid Ali³ · Said Karim Shah¹ · Yaseen Iqbal³ · Md. Abdul Aziz²

Received: 25 May 2020 / Accepted: 31 July 2020 / Published online: 9 August 2020
© Springer Science+Business Media, LLC, part of Springer Nature 2020

Abstract

Single-phase lead-zirconate-titanate (PZT) perovskite nanofibers, with $\text{Pb}(\text{Zr}_{0.5}\text{Ti}_{0.5})\text{O}_3$ composition were synthesized using the electrospinning technique. Poly-vinyl-pyrrolidone (PVP) was used as viscosity controller, size and uniformity of the $\text{Pb}(\text{Zr}_{0.5}\text{Ti}_{0.5})\text{O}_3$ nanofibers were optimized against different PVP concentrations. The results showed that PVP concentrations play a significant role in the fabrication, homogeneity, uniformity, porosity, and particularly in the diameter of PZT nanofibers. SEM and XRD results revealed the formation of single-phase $\text{Pb}(\text{Zr}_{0.5}\text{Ti}_{0.5})\text{O}_3$ nanofibers at 600 °C with an average diameter of ~96 nm. The prepared PZT nanofibers exhibited a significantly wide bandgap (~3.5 eV) and a high dielectric-constant (~1827). The device of single-phase PZT nanofibers was fabricated on interdigitated electrodes to study the current–voltage, impedance spectroscopy, and dielectric characteristics of the PZT nanofibers. The current–voltage characteristics of the fabricated device with PZT nanofibers showed non-ohmic properties. The non-linear I – V characteristics at temperatures between 308 and 408 K indicate two distinct regions. Impedance spectroscopy indicated the presence of non-ideal Debye type behavior in $\text{Pb}(\text{Zr}_{0.5}\text{Ti}_{0.5})\text{O}_3$ nanofibers and was ascribed to the existence of heterogeneity in the sample. The measured capacitances were assigned to two electro-active regions in the prepared $\text{Pb}(\text{Zr}_{0.5}\text{Ti}_{0.5})\text{O}_3$ nanofibers. A proto-type piezoelectric nanogenerator based on PZT nanofibers was fabricated to study the piezoelectric properties of $\text{Pb}(\text{Zr}_{0.5}\text{Ti}_{0.5})\text{O}_3$ nanofibers. PZT nanofibers were aligned on interdigitated electrodes of silver wire, which demonstrated piezoelectric performance and delivered an output voltage of ~40 V under periodic stress applications.

1 Introduction

Ever since the demonstration of earliest nanogenerator utilizing piezoelectric nanowires for transforming mechanical energy into electricity by Wang et. al. [1], excessive research interest has been carried out to develop numerous

approaches for energy harvesting [2]. Nanogenerators based on piezoelectric nanofibers are considered potential renewable energy sources for harvesting energy. These nanogenerators employ a self-powering approach for a maintenance-free and sustainable process of portable electronics and nanosystems [3]. Recently Gou et. al. [4] developed piezoelectric nanogenerator and enhance its current density using a three-dimensional intercalation electrode. Being an environment-friendly and green source of energy, this new paradigm in nanotechnology has drawn increased research attention of the scientific community over the past few years.

Currently, the formation of 1D nanostructures such as nanofibers, nanorods, nanotubes, nanowires perovskite ceramics, have opened new avenues in the field of nanotechnology. Among ceramic perovskites, polycrystalline ferroelectric ceramics such as barium-titanate (BaTiO_3), doped zinc-oxide (ZnO), and PZT nanofibers have been reported [5, 6] as promising candidates for unique piezoelectric applications. Thanks to their high dielectric constants (830–1470), high coupling (0.6–0.7), high charge sensitivity, high density (7.6–7.7 g/cm³) with nanocrystal grains of an average

Khizar Hayat and Syed Shaheen Shah have equally contributed to this work.

✉ Syed Shaheen Shah
syedshaheen.shah@kfupm.edu.sa

✉ Yaseen Iqbal
dryaseeniqbal@yahoo.co.uk

¹ Department of Physics, Abdul Wali Khan University Mardan, Mardan, KP 23200, Pakistan

² Center of Research Excellence in Nanotechnology (CENT), King Fahd University of Petroleum & Minerals, KFUPM, Box 5040, Dhahran 31261, Saudi Arabia

³ Materials Research Laboratory, Department of Physics, University of Peshawar, Peshawar 25120, Pakistan

diameter of 10 nm, high Curie point of around 1000 K, and clean noise-free frequency response [7, 8]. Owing to their prominent properties and application potential, piezoelectric materials are generally utilized in several applications, for example, nano-electromechanical systems, sensors and actuators, micro-electromechanical systems, nonvolatile-ferroelectric-memory devices, and nanogenerators [9–12]. PZT-based ceramics are perhaps one of the most significant classes for piezoelectric materials, due to their noteworthy piezoelectric performances. Its piezoelectric and dielectric performance is more reliable for the nanogenerator applications due to its directional behavior [13, 14]. PZT provides fast response to the applied voltage as well as to the load and has 2–4 times greater values of a piezoelectric constant as compared to semiconductor kind of piezoelectric nanofibers and nanowires, producing PZT as an ideal material for nanogenerator applications [15, 16]. Due to the prominent applications, brittle nature, and good piezoelectric performances, there is an emerging interest throughout the world for the production of large scale and mechanically flexible PZT nanofibers for nanogenerator applications [17–20].

Nanogenerators made of piezoelectric nanofibers are expected to work as substantial, easily usable, and inexhaustible energy supplies. For example, it is difficult to change the battery for a sensor on the wing of an aircraft or a satellite; however, devices which are hard-to-access can be self-powered. Moreover, an understanding of the fabrication of piezoelectric nanofibers and evaluating its electrical and mechanical properties will help with the energy harvesting at the nanoscale, which is still lacking. In nanotechnology, most of the research work is focused upon the advancement of cost-effective and mass production processes to prepare one dimensional (1D) nanostructured materials such as nanowires, nano-whiskers, nanorods, nanofibers, and nanotubes [21–24]. These nanostructures have a wide range of vital applications in the field of nanotechnology for manufacturing portable electronic devices. The core track of current research is also focused upon techniques to fabricate nanoscale counterparts of piezoelectric ceramics and to transform these materials into nanoscale devices. Keeping in view the attractive characteristics of 1D piezoelectric nanofibers (such as large specific surface area (SSA), high porosity, long length, and flexible nature), a number of applications have been proposed such as power generators at the nanoscale, gas storage units, optoelectronic components, fluidic devices, optical devices, optical waveguides, bioreactors, and tissue engineering scaffolds [25, 26]. Technologies based on energy harvesting materials, engineered to miniature sizes and at the same time still improving the energy supplied to stretchable electronics, implantable sensors, portable devices, and wireless electronics, are extensively desired [27]. Nanogenerators based on piezoelectric nanofibers have been extensively used for powering such

technologies by converting mechanical energy into electrical energy. Still, the piezoelectric voltage constant of semiconductor-piezoelectric nanofibers in most of the available piezoelectric-nanogenerators in the literature [28, 29] is lower than PZT-based nanofibers.

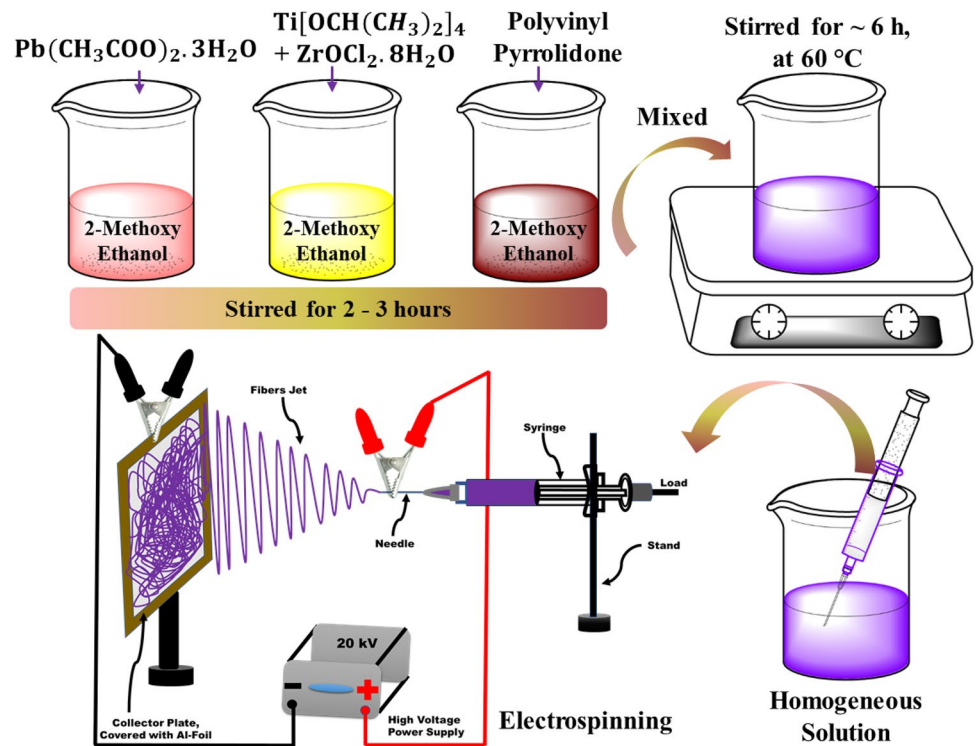
Here we report, the synthesis of 1D piezoelectric $\text{Pb}(\text{Zr}_{0.5}\text{Ti}_{0.5})\text{O}_3$ nanofibers at optimum processing conditions for piezoelectric nanogenerator applications using a versatile, simple, cost- and time-effective, and mass production electrospinning technique. The current–voltage (I – V), impedance spectroscopy, and dielectric characteristics of the prepared $\text{Pb}(\text{Zr}_{0.5}\text{Ti}_{0.5})\text{O}_3$ nanofibers were investigated through the fabrication of a single-phase PZT nanofibers-based device on interdigitated silver electrodes. The I – V characteristics of the fabricated device with $\text{Pb}(\text{Zr}_{0.5}\text{Ti}_{0.5})\text{O}_3$ nanofibers showed non-ohmic properties. The piezoelectric performance of $\text{Pb}(\text{Zr}_{0.5}\text{Ti}_{0.5})\text{O}_3$ nanofibers were studied by fabricating a proto-type piezoelectric-nanogenerator based on PZT nanofibers. PZT-nanofibers with an average-diameter of ~ 96 nm were aligned on interdigitated electrodes of silver wire, which demonstrated piezoelectric performance and delivered an output voltage of ~ 40 V under periodic stress applications. The fabrication of piezoelectric nanogenerators is expected to help in the development of a relatively more economical electricity production system. The findings are also expected to be academically valuable for the relevant community.

2 Experimental details

2.1 Preparation of $\text{Pb}(\text{Zr}_{0.5}\text{Ti}_{0.5})\text{O}_3$ nanofibers via electrospinning

Electrospinning technique has been used for the synthesis of $\text{Pb}(\text{Zr}_{0.5}\text{Ti}_{0.5})\text{O}_3$ nanofibers. Lead acetate trihydrate [$\text{Pb}(\text{CH}_3\text{CO}_2)_2 \cdot 3\text{H}_2\text{O}$], zirconium(IV) oxychloride octahydrate [$\text{ZrOCl}_2 \cdot 8\text{H}_2\text{O}$], and titanium(IV) isopropoxide [$\text{Ti}[\text{OCH}(\text{CH}_3)_2]_4$] were utilized as the starting materials while 2-methoxy ethanol [$\text{C}_3\text{H}_8\text{O}_2$] was used as a solvent. In a typical procedure, 3.8 g of $\text{Pb}(\text{CH}_3\text{CO}_2)_2 \cdot 3\text{H}_2\text{O}$, 1.6 g of $\text{ZrOCl}_2 \cdot 8\text{H}_2\text{O}$, and 1.4 g of $\text{Ti}[\text{OCH}(\text{CH}_3)_2]_4$ were separately dissolved in 10 ml of 2-methoxy ethanol and stirred for ~ 2 to ~ 3 h. A specific amount (10–30 wt%) of polyvinylpyrrolidone (PVP) ($M_w \approx 1,300,000$) was dissolved in 10 ml of 2-methoxy ethanol and stirred for ~ 30 min. Several experiments were conducted at different concentrations of PVP for optimization. After vigorous stirring, all the prepared solutions were mixed and carefully stirred at 60°C for ~ 6 h to produce a viscous and homogeneous mixture solution. Figure 1 shows the schematic representation for the solution preparation process.

Fig. 1 Schematic showing the solution preparation for electrospinning of PZT/PVP composite nanofibers and the electrospinning process



The final viscous and homogenous solution was loaded into a plastic-syringe used as a solution mediator in the electrospinning technique. A high voltage direct-current power-supply of 20 kV that is used to generate a high electric-field between the needle tip of the syringe and fiber collector plate. The needle was connected to the positive terminal while the fiber collector plate was connected to the negative terminal of the high voltage power supply. The fiber collector plate was covered by the aluminum (Al) foil to collect the produced composite nanofibers. The collector covered with Al-foil was placed at a distance of ~ 14 cm from the tip of the syringe needle. Due to the application of load through the syringe and high voltage power supply between the collector and needle, a continuous jet of composite fibers was produced from the viscous solution and deposited on the Al-foil. The schematic representation for the electrospinning process used in the preparation of PVP/PZT composite fibers is shown in Fig. 1.

The composite nanofibers deposited on aluminum foil were kept in an electric oven for drying at 90 °C for 10 h. The composite nanofibers were collected from the aluminum foil and kept in a crucible for further heat treatment and then thermally treated in a chamber furnace for eight hours and were then cooled. A rate of 5 °C/min was set both for heating and cooling, and the calcination temperature was set at 600 °C, where PVP and other volatile components were removed through high temperature. Analytical techniques, namely energy dispersive-X-ray (EDS) spectroscopy, scanning-electron-microscopy (SEM),

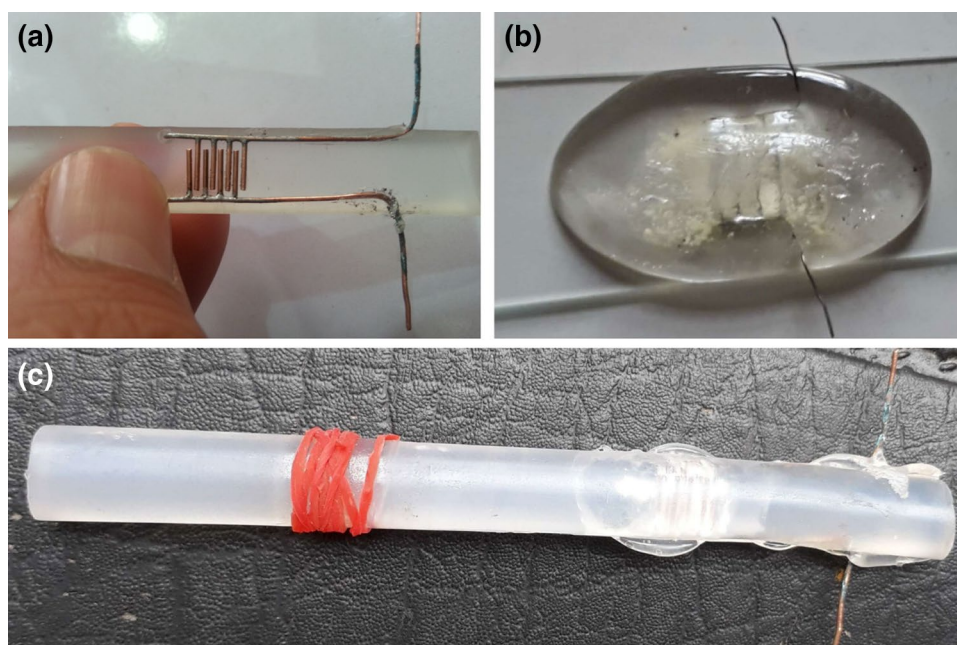
thermogravimetric-analysis (TG/DTA), Fourier-transform-infrared (FTIR) spectroscopy, X-ray diffraction (XRD), and ultraviolet–visible (UV–VIS) spectroscopy, were applied to characterize the prepared materials. Keithley 2410 sourcemeter, Agilent LCR meter (E4980A), and Keithley 2182A Nanovoltmeter were used for I – V , impedance, and piezoelectric analyses, respectively.

2.2 Fabrication of $\text{Pb}(\text{Zr}_{0.5}\text{Ti}_{0.5})\text{O}_3$ nanofibers based nanogenerator

The single phase $\text{Pb}(\text{Zr}_{0.5}\text{Ti}_{0.5})\text{O}_3$ nanofibers calcined at 600 °C with an average diameter of ~ 96 nm were deposited on interdigitated electrodes of silver fine wires and packed with a soft-polymer on a glue gun stick flexible substrate. The evaluated output voltage in compliance with the periodic-stress applications to the soft-polymer was ~ 40 V. The proto-type nanogenerator device was engineered by utilizing the prepared PZT nanofibers as a piezoelectric material. The uniform and continuous PZT nanofibers with an average diameter of ~ 96 nm were deposited on the pre-prepared interdigitated silver fine wire electrodes, which were assembled on a glue gun stick flexible substrate as shown in Fig. 2a. The adjacent electrodes were separated by a distance of ~ 0.7 mm in the interdigitated device.

The interdigitated electrodes of silver fine wires were connected by the conductive wires to transport the harvested power to an external circuit. Figure 2a–c illustrated the fabricated nanogenerator device, where the prepared

Fig. 2 **a** Photograph of the interdigitated electrodes used for nanogenerator, **b** cross sectional view of the integrated PZT nanofibers in the proto-type nanogenerator and **c** proto-type nanogenerator used for cantilever applications



PZT nanofibers are working in the longitudinal-mode, and an alternating pressure can be applied on the top-surface of the device. The pressure applied on the top-surface is transported to the aligned PZT nanofibers via the flexible matrix which results in the generation of charges owing to the combined bending and tensile stresses in the $\text{Pb}(\text{Zr}_{0.5}\text{Ti}_{0.5})\text{O}_3$ nanofibers. A potential gap between the two adjacent electrodes of the interdigitated device is thus produced by the separation of charges. The interdigitated electrodes might improve the output power of the nanogenerator, where the PZT nanofibers between every pair of adjacent-electrodes act as a unit cell which were connected in parallel. When the PZT nanofibers subject to the applied stresses, the electrons generated could transfer through the electrodes. In order to prevent unnecessary stresses on the PZT nanofibers and to minimize the risk of damaging the electrical connection of the electrodes, the flexible substrate was slightly melted at slow heating along with the nanogenerator and then cooled for a rigid mechanical backing as shown in Fig. 2b. This proto-type nanogenerator can be used as a cantilever for the periodic generation of power, for this reason, the nanogenerator was imbedded at the one end of the glue stick, which can be used as a cantilever (Fig. 2c).

3 Results and discussion

3.1 Microstructural and morphological analysis

The microstructural analysis of both the prepared PVP/PZT composite fibers and its derived single-phase $\text{Pb}(\text{Zr}_{0.5}\text{Ti}_{0.5})\text{O}_3$ nanofibers were characterized using a

scanning-electron-microscope (SEM, JSM-5910, JEOL), operated at an accelerating-voltage of 15 kV. The SEM micrographs were taken with differentiation magnifications of the nanofibers. The elemental-analysis of the prepared samples was carried out using EDS analysis. Different PVP concentrations (10–30 wt%) were used for the optimized morphology and diameter of the required nanofibers. For the diameter estimation, the microstructural images were analyzed using *ImageJ* software. Calcination temperature of 600°C was used for the single-phase formation of the PZT nanofibers.

The most significant parameters related to the nanofibers produced via electrospinning are their controlled morphology and diameter. According to Sirc et al. [30], the SSA of nanofibers increases 1000 times once the diameter of nanofiber decreases from 100 μm to 100 nm. This implies that a decrease in the weight of materials with greater efficiency is required for an equivalent SSA. The small-diameter and uniform-morphology make the nanofibers to be suitable for many applications such as catalysts, filtrations, sensors, and nanogenerators [31]. The morphology and diameter of nanofibers can be influenced by varying many parameters such as flow-rate of the solution, surface-tension, gauge of the needle, polymer concentrations, applied voltage, and current. Among these parameters, the polymer concentrations play an essential role in the morphology and diameter of nanofibers [32].

To support this prediction on the synthesis of nanofibers by electrospinning, Shenoy et al. [33] proposed a model for concentrated or moderately concentrated solutions, in which the entanglement number $(n_e)_{\text{soln}}$ in solution can be defined as

$$(n_e)_{\text{soln}} = \frac{(\phi_p M_w)}{M_e} \quad (1)$$

where, the molecular-weight of the polymer is represented by M_w , ϕ_p is the volume fraction, and M_e is entanglement-molecular-weight of the polymer in solution. According to Eq. 1, it is possible to conclude that morphological variations during the electrospinning process using the same polymer and molecular weight, can be controlled by polymer concentration in the solution. It has been proposed that, during the electrospinning process, a decrease of the polymer concentration in the solution results in the following variations in the nanofibers morphology: beads only, beads with emerging nanofibers, and nanofibers only. An $(n_e)_{\text{soln}}$ of 2 for a polymer solution is equivalent to about 1 entanglement-per-chain, whereas, it is usually required to use a polymer solution with an $(n_e)_{\text{soln}}$ larger than 3.5 for the fabrication of pure fibers by electrospinning. There will be a conversion from beaded fibers to pure fibers if the $(n_e)_{\text{soln}}$ is between 2 and 3.5 and if the $(n_e)_{\text{soln}}$ is less than 2 then there will be no fiber (only beads) [33, 34]. Here we investigate how the concentrations of PVP influence the diameter and morphology of the prepared PZT nanofibers.

Figure 3 illustrates the SEM micrographs for the variation of diameter and morphology of the as-prepared PVP/PZT composite nanofibers with the effect of different PVP concentrations. It was shown that higher concentrations of the PVP resulted in more beads and become

agglomerated. Beads, beads with emerging nanofibers, non-uniform nanofibers, and uniform pure nanofibers have been obtained from the PVP concentrations of 30 wt%, 20 wt%, 15 wt%, and 10 wt%, respectively. As illustrated in Fig. 3a, b, the as-spun nanofibers with 30 wt% and 20 wt%, exhibited only agglomerated beads and nanofibers with the combination of beads (marked with dotted circles), respectively. Decreasing the PVP concentrations gave an improvement for 15 wt%, (Fig. 3c), but smooth and continuous nanofibers were still not obtained. Further decrease in the PVP concentration to 10 wt% produced continuous nanofibers with uniform morphology and a smaller diameter of 130 ± 22 nm (Fig. 3d).

The SEM analyses for the PZT nanofibers prepared after calcination at 600 °C with different PVP concentrations in the solutions are displayed in Fig. 4. Calcination was carried out at 600 °C with the aim for single-phase formation of the $\text{Pb}(\text{Zr}_{0.5}\text{Ti}_{0.5})\text{O}_3$ nanofibers along with the morphological variations at this calcination temperature. Figure 4a shows the SEM micrograph of the agglomerated beads prepared with 30 wt% PVP concentration and calcined at 600 °C, which represents that the beads are completely compressed with each other without the formation of any specific morphology. While from the calcination of beads with emerging nanofibers for 20 wt% PVP concentration, it can be seen in Fig. 4b that the beads have almost vanished at 600 °C resulted in non-uniform nanofibers with a larger diameter.

Figure 4c, d show a decrease in the diameter of nanofibers from ~ 198 to ~ 105 nm and from ~ 121 to ~ 96 nm with a

Fig. 3 SEM micrographs of the as-spun PVP/PZT composted nanofibers, with PVP concentration of 30 wt% (a), 20 wt% (b), 15 wt% (c), and 10 wt% (d)

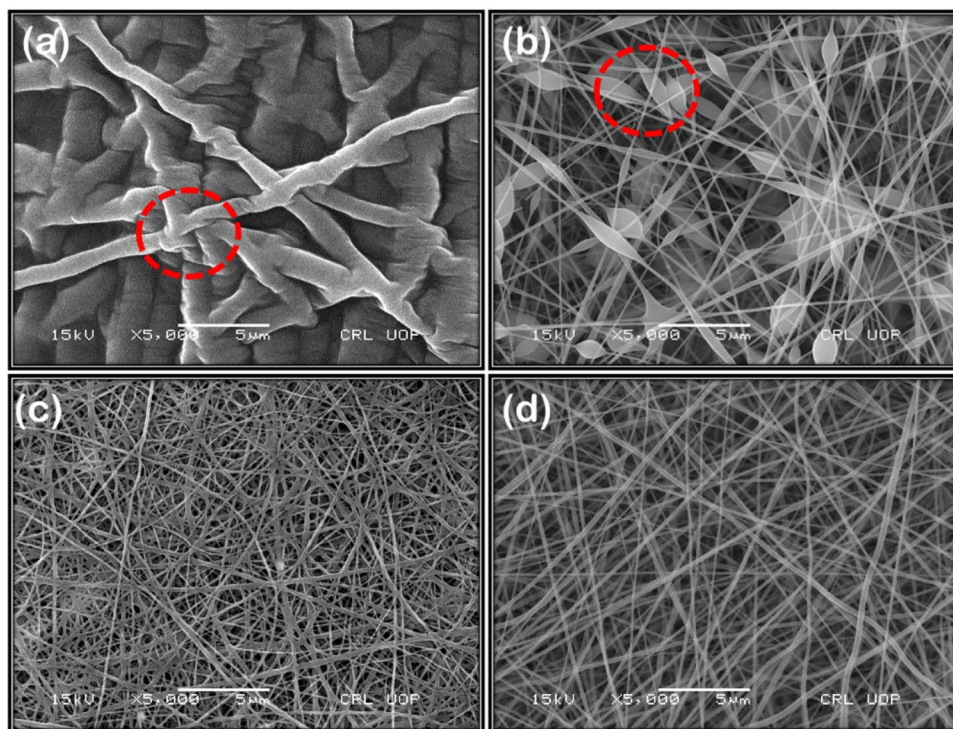
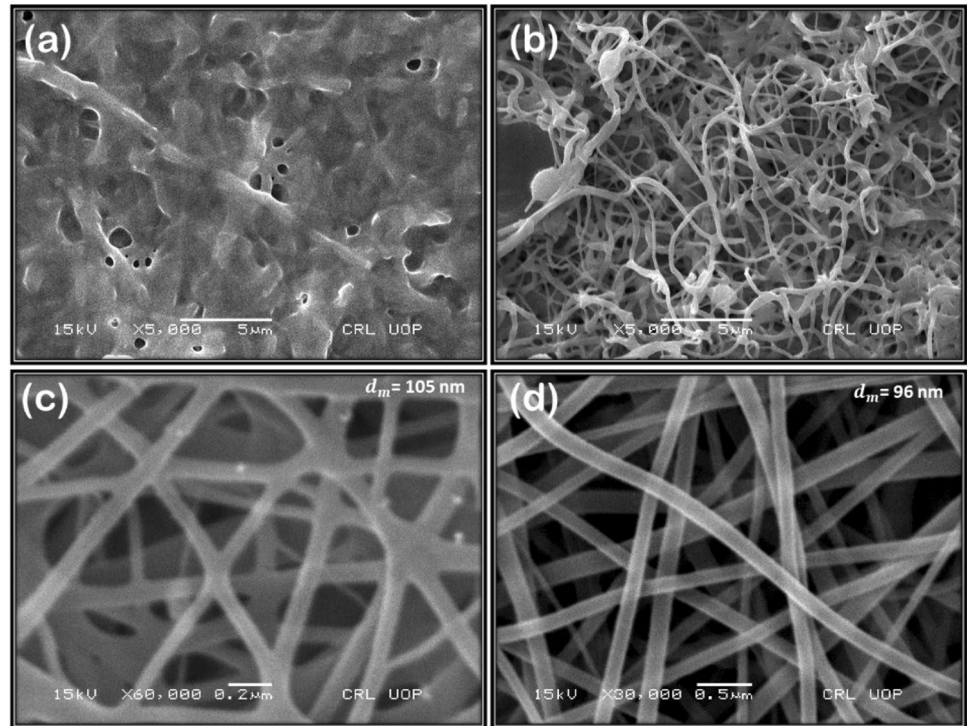


Fig. 4 SEM micrographs of the PZT nanofibers calcined at 600 °C, with PVP concentration of 30 wt% (a), 20 wt% (b), 15 wt% (c), and 10 wt% (d)

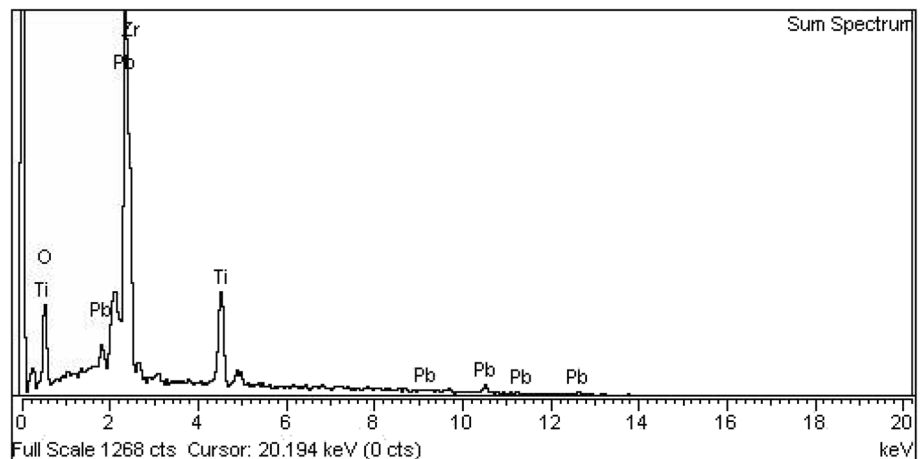


calcination temperature of 600 °C for the PVP concentration of 15 wt% and 10 wt% respectively. This shrink in the diameter of nanofibers after calcination at 600 °C is attributed to the decomposition of PVP, removal of organic residuals, and the crystallization of PZT [31, 35]. It can also be seen from the SEM results, that after calcination at 600 °C the nanofibers became porous. This uniform and porous nature provide an important platform to enhance the mechanical behavior of piezoelectric nanofibers. The dielectric-constant values of the PZT nanofibers have been reported to increase with the increase in the porosity of the sample [36]. The optimized nanofibers with an average diameter of ~96 nm were produced in the current study after the calcination of

PVP/PZT composite nanofibers (10 wt% PVP concentration) at 600 °C. As uniform and small diameter are essential for nanofibers to have promising properties, such as excellent mechanical performances, high SSA, and flexible structures [37]. Therefore, it was concluded that the nanofibers have the optimized ratio was selected for further analysis and characterizations.

Figure 5 shows the EDS spectra of $\text{Pb}(\text{Zr}_{0.5}\text{Ti}_{0.5})\text{O}_3$ nanofibers calcined at 600 °C, indicating the relative quantity of the principal elements of PZT, i.e. Pb, Zr, and Ti. EDS analysis was carried out to determine the purity of the synthesized PZT nanofibers. It can be observed that there is no impurity in synthesized nanofibers, demonstrating the

Fig. 5 The EDS spectrum of $\text{Pb}(\text{Zr}_{0.5}\text{Ti}_{0.5})\text{O}_3$ nanofibers, calcined at 600 °C



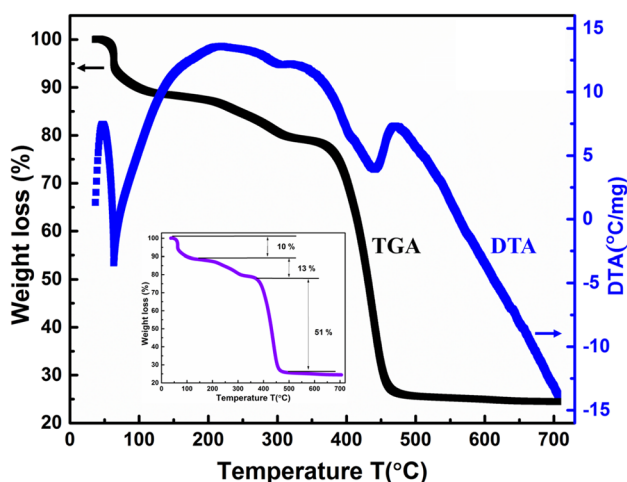


Fig. 6 The TG/DTA curves of the as-spun PZT nanofibers

reliability of the electrospinning process and the high purity of the precursor materials. The presence of a constituent element in PZT nanofibers is indicated by the peaks of Pb, Zr, Ti, and O. So, it could be confirmed that the PZT nanofibers were formed.

A sample of composite nanofibers, dried at 90 °C, was used for TG/DTA analysis. The TG/DTA for $\text{Pb}(\text{Zr}_{0.5}\text{Ti}_{0.5})\text{O}_3$ were carried out from room temperature to 600 °C with a heating and cooling of 5 °C/min, as shown in Fig. 6. The TGA curve exhibits three significant losses; the first one appeared between 25 and 102 °C (~10%) is attributed to the evaporation of physically absorbed water and the solvent, the second one located between 102 and 380 °C (about 13%) is due the removal of chloride and nitrate groups from the PVP/PZT composite nanofibers and the third major weight loss occurring between 380 and 480 °C (about 51%) is due to the major decomposition of PVP main chain [24, 35]. These observations can be confirmed from the inspection of the DTA curve. There are three major peaks in the DTA curve at 156 °C, 346 °C, and 480 °C. The decomposition of the PZT composite nanofibers is characterized by one endothermic peak between 120 and 156 °C owing to the evaporation of physically-absorbed water and the solvent and two main exothermic peaks. One exothermic peak in the range of 156–400 °C is ascribed to the decomposition of PVP main chain and the evaporation of volatile-species accompanied by a massive weight loss. The last exothermic peak is assigned to the formation of the perovskite phase of PZT [38]. The actual crystallization temperature for the formation of single-phase perovskite was determined from TG/DTA analysis.

Figure 7 present XRD spectra of the prepared pure PVP, composite-nanofibers heat treated at 90 °C, and single-phase $\text{Pb}(\text{Zr}_{0.5}\text{Ti}_{0.5})\text{O}_3$ nanofibers calcined at 600 °C. For comparison the standard XRD diffractogram of the single-phase

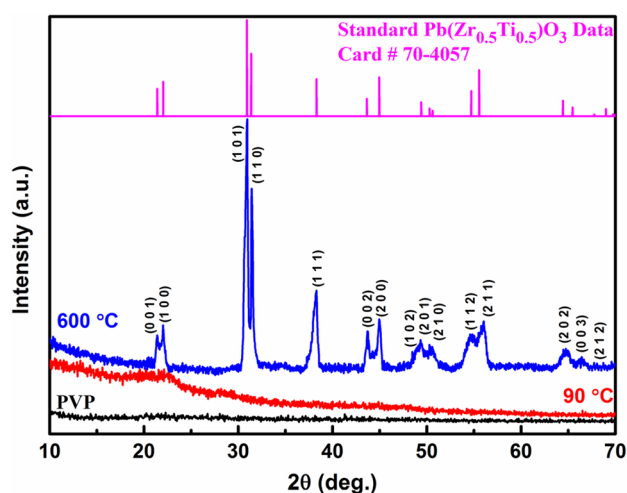


Fig. 7 XRD patterns of pure-PVP and the prepared samples heat-treated at 90 and 600 °C with the standard XRD spectrum of single-phase $\text{Pb}(\text{Zr}_{0.5}\text{Ti}_{0.5})\text{O}_3$ ceramics (JCPDS Card# 70–4057)

$\text{Pb}(\text{Zr}_{0.5}\text{Ti}_{0.5})\text{O}_3$ ceramics (JCPDS Card # 70–4057) is displayed on the top of Fig. 7. The XRD spectra recorded for the pure PVP and sample heat-treated at 90 °C were almost the same and shows typical amorphous nature, as no crystalline peaks could be seen on these spectra. To identify the crystalline peaks and single-phase formation of $\text{Pb}(\text{Zr}_{0.5}\text{Ti}_{0.5})\text{O}_3$ nanofibers, the sample calcined at 600 °C was used for XRD analysis by operating the PANalytical X'Pert³ Powder X-ray diffractometer. The 2θ scan ranging from 10° to 70° was recorded for the samples with an angle increment of 0.01°. Fifteen (15) broad diffraction peaks were detected on the XRD spectrum of sample heat treated at 600 °C, which matched the (001), (100), (101), (110), (111), (022), (200), (102), (201), (210), (112), (211), (202), (003), and (212) reflections of the standard XRD diffractogram (JCPDS card# 70–4057) for single phase $\text{Pb}(\text{Zr}_{0.5}\text{Ti}_{0.5})\text{O}_3$ nanofibers. These broad XRD peaks showed the formation of single-phase $\text{Pb}(\text{Zr}_{0.5}\text{Ti}_{0.5})\text{O}_3$ nanofibers at 600 °C and indicate the presence of the nanocrystalline phase [38].

Further characterization by FTIR was carried out to investigate the exact perovskite formation of PZT nanofibers at 600 °C. Figure 8 illustrates the FTIR spectra of pure-PVP and the prepared samples heat-treated at 90 and 600 °C. The FTIR spectrum of pure PVP shows five dominant absorption peaks. The two broad peaks may be attributed to the stretching-vibrations of the C–H bond ($\nu_{\text{C-H}}$) observed ~2950 cm^{-1} and a hydroxyl group ($\nu_{\text{O-H}}$) observed at ~3450 cm^{-1} [24, 39]. The other three sharp peaks at 1270 cm^{-1} , 1421 cm^{-1} , and 1650 cm^{-1} may be related to the stretching of $\nu_{\text{C-N}}$, $\nu_{\text{C-H}}$, and $\nu_{\text{C=O}}$ bonds, respectively [24, 39]. While in the case of PZT/PVP composite nanofibers heat-treated at 90 °C, all the peaks appeared in the FTIR spectrum are still matching with the peaks of pure PVP, however with comparatively

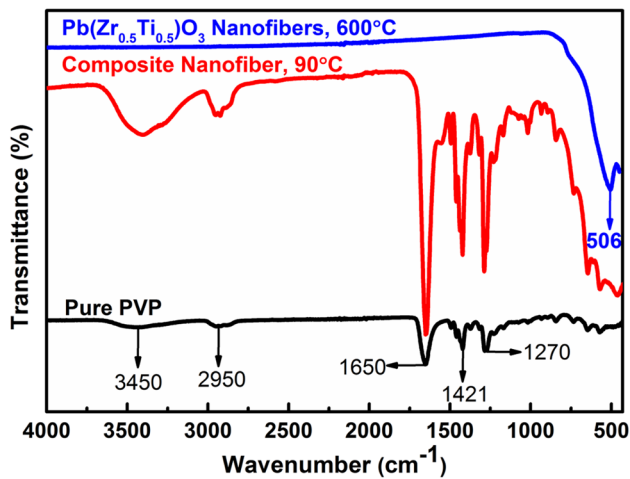


Fig. 8 The FTIR spectra of pure PVP and the prepared samples heat-treated at 90, and 600 °C

lower-intensities. The FTIR spectrum for the single-phase PZT nanofibers calcined at 600 °C exhibited no association of PVP, indicated the complete decomposed of PVP and the oxidation of other volatile components. The one additional prominent peak noticed at 506 cm^{-1} is a sign of the preparation of a new structure, i.e. PZT crystal [40].

3.2 Optical properties

Based on the principle of electronic transitions, UV–Vis spectroscopy is used to measure various optical characteristics of the ultraviolet, visible light, and infrared radiations that are emitted by or reflected from and or passed through a sample. One of the powerful spectroscopic techniques is

absorption because absorption can be used to evaluate the bandgap energy (E_g) of samples very efficiently. E_g not only depends on the stoichiometry of material but also on its crystallinity. That is the reason why the estimation of E_g is considered very significant in the characterization of nanomaterials [41]. Many techniques have been used to extract the value of bandgap energy, depending upon the nature of a material [42–44]. Tauc plot from the absorption spectrum in the UV–Vis spectroscopy is one such technique, which is a very simple and effective way to estimate E_g of nanocrystalline samples.

To estimate the E_g of $\text{Pb}(\text{Zr}_{0.5}\text{Ti}_{0.5})\text{O}_3$ nanofibers, the absorption spectrum was obtained using UV–Vis–NIR PerkinElmer lambda 1050/URA spectrometer in a wavelength range of 200–500 nm, as shown in Fig. 9a. The Bandgap energy value was determined from the Tauc plot of $(\alpha h\nu)^2$ versus photon energy ($h\nu$) using the UV–Vis spectrum. The absorption coefficient (α) varies as a function of frequency (ν), according to the following equation [45].

$$\alpha h\nu = (h\nu - E_g)^n \quad (2)$$

where $h\nu$ is the photon energy and E_g is the bandgap energy; $n = 2$ for direct transitions and $n = 1/2$ for indirect transitions. Since PZT is known to exhibit direct bandgap [46], therefore the bandgap energy was obtained by plotting $(\alpha h\nu)^2$ versus photon energy ($h\nu$) as presented in Fig. 9b. The bandgap energy of the $\text{Pb}(\text{Zr}_{0.5}\text{Ti}_{0.5})\text{O}_3$ nanofibers was estimated as ~ 3.5 eV, which is in good agreement with the reported bandgaps of 3.4, 3.54, and 3.65 eV for different compositions of $\text{Pb}(\text{Zr}_{1-x}\text{Ti}_x)\text{O}_3$ [46–48]. This result also suggests that PZT has a direct and wide bandgap, and materials having a direct and wide bandgap are very effective for large

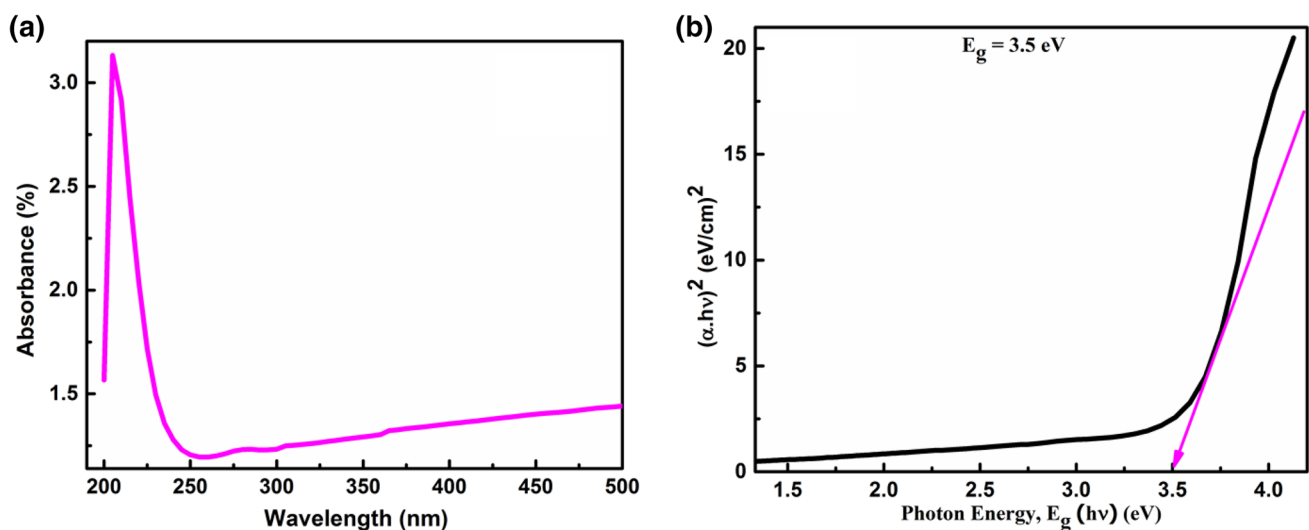


Fig. 9 a UV–Vis spectrum and b Tauc plot of $\text{Pb}(\text{Zr}_{0.5}\text{Ti}_{0.5})\text{O}_3$ nanofibers

piezoelectric effects in nanogenerators [49, 50]. Similarly, wide bandgap semiconductors are supposed to revolutionize the next generation of power electronics and clean energy innovations [51].

3.3 Electrical properties

The impedance spectroscopy data were taken from room temperature (308 K) to high temperature (398 K) with a frequency sweep from 20 Hz to 2 MHz by E4980A Precision LCR Meter, (Keysight). Figure 10a, b demonstrate the complex-impedance (Z' vs. Z'') Nyquist plots of $\text{Pb}(\text{Zr}_{0.5}\text{Ti}_{0.5})\text{O}_3$ nanofibers, measured at selected temperatures (308–398 K) as a function of frequency (20 Hz–2 MHz). The impedance spectra are characterized by the presence of semi circular arcs for which the pattern changes with the increase in temperature. Every semi circular arc in the Nyquist plot may

be ascribed to a parallel combination of capacitance and resistance. At every temperature, the Nyquist plot illustrates the over lapped and depressed semi circular arcs with center that lies beneath the Z' -axis. This specifies two distinct characteristics of the $\text{Pb}(\text{Zr}_{0.5}\text{Ti}_{0.5})\text{O}_3$ nanofibers. (i) The over lapped nature of the semi circular arcs reveal the existence of more than one relaxation phenomena in $\text{Pb}(\text{Zr}_{0.5}\text{Ti}_{0.5})\text{O}_3$ nanofibers at each temperature. These relaxation-phenomena are related to different electro-active regions. Because of the over lapped nature of the semi circular arcs, the related change in the relaxation times, $\tau = RC$, is negligible. (ii) The depressed nature of the semi circular arcs implies the non-ideal debye type characteristic of the $\text{Pb}(\text{Zr}_{0.5}\text{Ti}_{0.5})\text{O}_3$ nanofibers and can be attributed to several factors. Which includes vacancies due to oxygen because of the stress strain phenomena in the lattice, nonstoichiometric distribution of oxygen, orientation of grains, and dangling

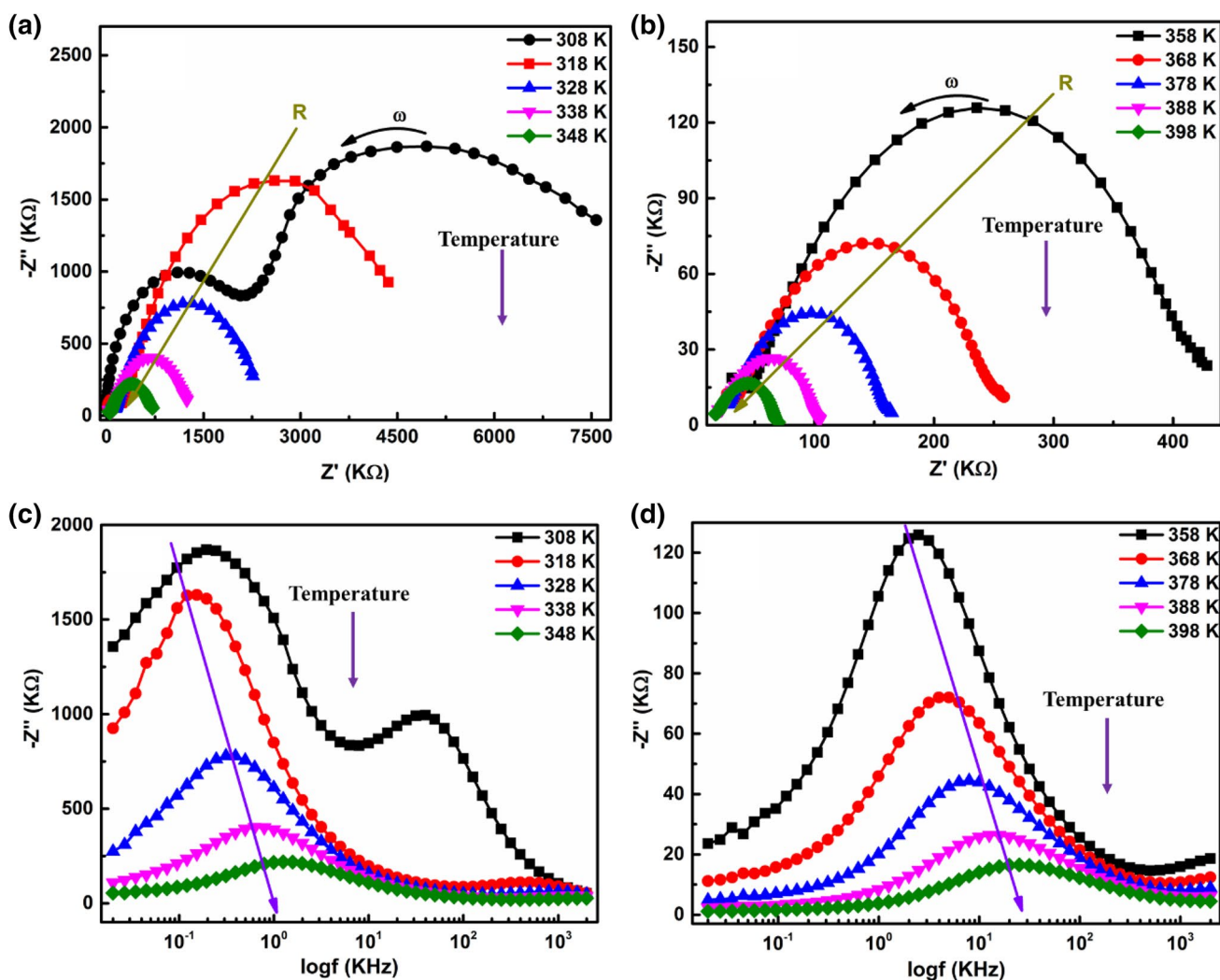


Fig. 10 a, b Nyquist plots, and c, d variation of imaginary part (Z'') as a function of frequency for $\text{Pb}(\text{Zr}_{0.5}\text{Ti}_{0.5})\text{O}_3$ nanofibers at selected temperatures

bonds at grain boundaries [23, 24]. The arrow (ω) shows the increase in frequency. At low frequency the intersection with Z' -axis of Nyquist-plots delivers total resistance of the $\text{Pb}(\text{Zr}_{0.5}\text{Ti}_{0.5})\text{O}_3$ nanofibers. Nyquist plot gives evidence regarding the electrical micro structure of the material in the shape of semi circular arcs and every semi circular arc signifies an electro-active region. It is demonstrated that with the rise in temperature, the radius of each semi circular arc shows a decreasing trend, which reveals a reduction in the resistivity of the sample with the increase in temperature of the $\text{Pb}(\text{Zr}_{0.5}\text{Ti}_{0.5})\text{O}_3$ nanofibers. This result suggests the semiconductor nature of the PZT nanofibers.

Figure 10c and d shows the difference in the imaginary part (Z'') of the complex-impedance as a function of frequency at selected temperatures for the $\text{Pb}(\text{Zr}_{0.5}\text{Ti}_{0.5})\text{O}_3$ nanofibers. This result demonstrates that at each temperature the plot exhibits peak and as the temperature increases the peak shift in the direction of high frequency with a broadening approach and a decrease in the height of the peak. This behaviour suggests a thermally activated dielectric-relaxation phenomenon in the PZT nanofibers and displays a reduction in the resistance with the increase in temperature [52]. A substantial peaks broadening with a rise in the temperature reveals the existence of a temperature dependent relaxation phenomenon in the PZT nanofibers. These dispersion-curves seem to merge at higher-frequency, which can be attributed to the accumulation of space-charge at lower-frequencies as well as its elimination at higher-frequencies [53].

The complex impedance plane plots are dominated by the most-resistive-regions and give minimal information for an electrically inhomogeneous material like the $\text{Pb}(\text{Zr}_{0.5}\text{Ti}_{0.5})\text{O}_3$ nanofibers. Therefore, combined spectroscopic-plots of the imaginary components of complex impedance (Z'') and electric-modulus (M'') are applied to investigate the electrically inhomogeneous nature of the PZT nanofibers. These results are beneficial in the direction that we can also probe the conductive regions having the smallest capacitance in parallel with the most resistive regions, as per our earlier report [54]. This mechanism is also useful to examine the relaxation time in the conductivity measurements. The combined spectroscopic-plot of M'' and Z'' vs. $\log(f)$ can be applied to investigate the impact of large resistance and the small capacitance, as proposed by Sinclair et al. [55].

The number of electro-active regions present in $\text{Pb}(\text{Zr}_{0.5}\text{Ti}_{0.5})\text{O}_3$ nanofibers, are presented in Fig. 11 by combined spectroscopic plots of M'' and Z'' , are typically determined in accordance with the number of peaks. The combined spectroscopic-plots of the Z'' and M'' at two different temperatures (308 K and 318 K) are shown in Fig. 11. In Fig. 11a, at 308 K, Z'' vs. $\log(f)$ plot shows two peaks that are moves in the direction of high frequency with the increase

of temperature. In M'' vs. $\log(f)$ spectrum, one prominent peak can be seen at 308 K which also shifts towards high frequency at 318 K. This is due to the experimental limitation of available frequency and temperature ranges which limits the investigations to get the grain effect with increasing temperature and electrode effect which can be seen at lower temperatures. This matter can be resolved through an increase in the applied frequency range, which is a limitation from the system. We can see from Fig. 11a and b, that both the observed peaks are situated at different frequencies, which suggest that these Debye peaks constitute two-different electro-active regions in the PZT nanofibers. At each temperature, the capacitance values were measured from the peaks of plots in M'' vs. $\log(f)$ and Z'' vs. $\log(f)$. Based on the measured capacitances, the existing two electro-active regions were given names as grain/bulk and grain-boundary.

Figure 11c shows the plots of grain boundary and bulk capacitance as a function of temperature. From this result, we observed that the capacitance of grain/bulk lies in the range of (10^{-11} – 10^{-12} F) while that of grain boundary lies in the range of (10^{-10} – 10^{-11} F), and these values are in accordance with the criterion proposed by Irvin et al. [56]. In this plot, the variation in capacitance of bulk/grain and grain boundaries is almost constant with temperature.

3.4 Dielectric properties

The dielectric-constant of the PZT nanofibers was measured from the real and imaginary parts of the complex impedance spectroscopy results by utilizing the following equation [57].

$$\epsilon = \frac{Z''}{(\omega C_0 |Z^*|^2)} \quad (3)$$

where, $C_0 (= \epsilon_0 A/d)$ is a constant, and the other terms in the equation have their typical meanings.

Figure 12 demonstrates the variation of dielectric constant (ϵ) as a function of the applied frequency of the PZT nanofibers at the applied temperatures (308–398 K). As shown in Fig. 12a the ϵ decreases with the increase in frequency. Initially, ϵ decreases sharply, and after that, it decreases smoothly. This decrease in ϵ , with an increase in frequency may be based on the dipole relaxation phenomenon [57]. The variation of ϵ with the applied temperature at various frequencies ranging from 10 kHz and 2 MHz is shown in Fig. 12b. It can be observed from this figure that the ϵ increases with increasing temperature of the system, which suggests that that thermally-activated dipoles might increase the polarization and consequently results in an increase in the ϵ of the system with the increase in temperature [58]. To acquire the piezoelectric material having a high ϵ value, attention must be paid to the ϵ at room temperature and at high frequency [59], therefore the dielectric constant

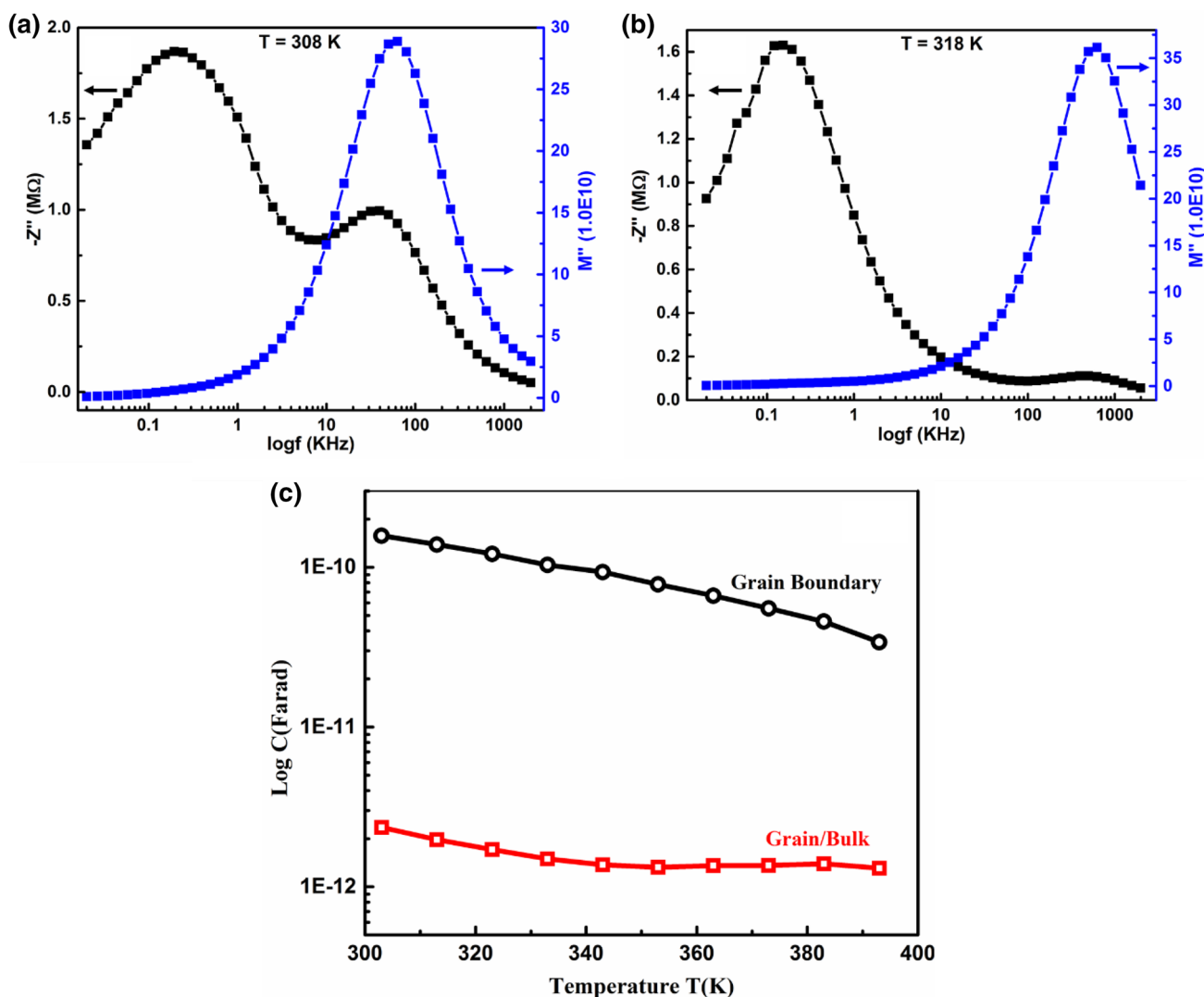


Fig. 11 Combined spectroscopic-plots for the imaginary parts of complex-impedance Z'' and electric-modulus M'' for PZT nanofibers corresponding to the experimental data at, 308 K (a), and 318 K (b),

and capacitance as a function of temperature for grain/bulk and grain boundary (c)

of $\text{Pb}(\text{Zr}_{0.5}\text{Ti}_{0.5})\text{O}_3$ nanofibers recorded at room temperature and at a high frequency 2 MHz is ~ 1827 . This high value of ϵ for $\text{Pb}(\text{Zr}_{0.5}\text{Ti}_{0.5})\text{O}_3$ nanofibers are in good agreement with the dielectric constants of PZT ceramics reported in literature [60, 61]. The dielectric-constant mainly ascertain the effectiveness and applicability of a piezoelectric materials as an actuator or a sensor [62].

3.5 Current–voltage (I – V) characteristics

Temperature-dependent I – V characteristics were performed to investigate the transport and conduction mechanisms present in $\text{Pb}(\text{Zr}_{0.5}\text{Ti}_{0.5})\text{O}_3$ nanofibers. The I – V characteristics of the nanogenerator based on $\text{Pb}(\text{Zr}_{0.5}\text{Ti}_{0.5})\text{O}_3$ nanofibers

are shown in Fig. 13. The I – V data were obtained at selected temperatures ranges from 308 to 408 K with a step of 10 K by Keithley Source meter (2410). During measurements, the given applied voltage range was -10 to 10 V. The I – V curves in Fig. 13a show that the current increases as temperature and voltage increase, which represents a typical semiconducting behavior. It is also clear from Fig. 13a that at the selected temperatures, the I – V curves are not linear in nature. According to the power-law $I \propto V^m$ [63], these results suggest that certain non-ohmic like behavior is present in $\text{Pb}(\text{Zr}_{0.5}\text{Ti}_{0.5})\text{O}_3$ nanofibers in the selected temperature range.

To explore the possible conduction mechanisms, present in the PZT nanofibers, we have plotted a double logarithmic plot as shown in Fig. 13b. It is clear from this result that there

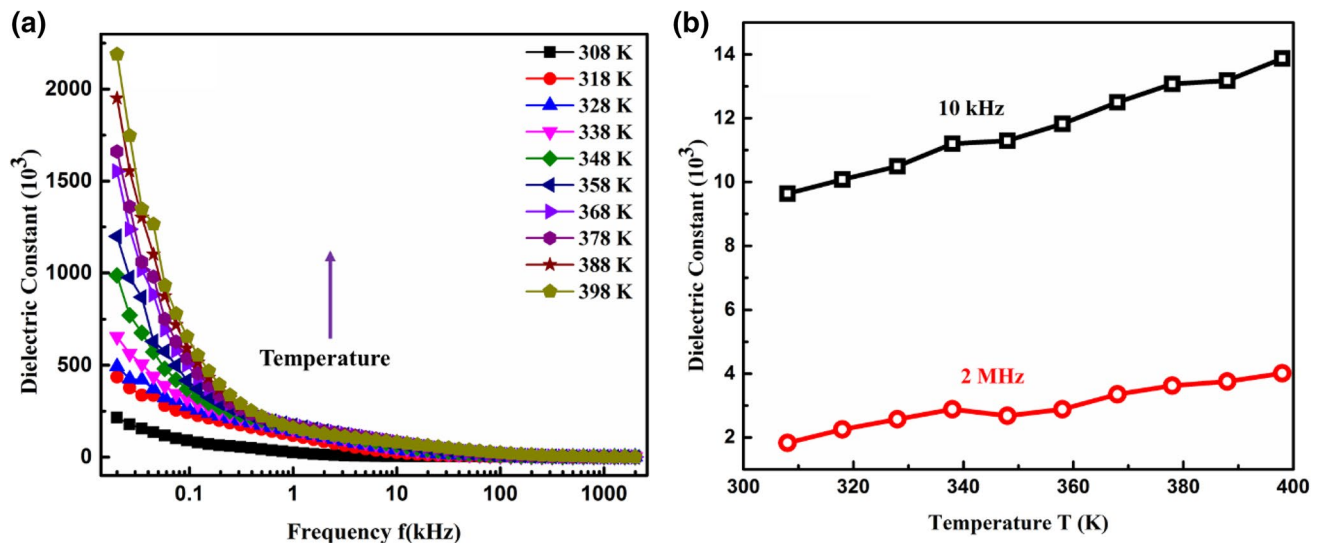


Fig. 12 The variation in dielectric-constant of the $\text{Pb}(\text{Zr}_{0.5}\text{Ti}_{0.5})\text{O}_3$ nanofibers as a function of **a** frequency at selected temperatures and **b** selected temperatures at frequency of 2 MHz and 10 kHz

are two-different regions, named as a region-I (low-voltage region) and region-II (high-voltage region). Following two different regions are responsible for two different types of conduction mechanisms in the $\text{Pb}(\text{Zr}_{0.5}\text{Ti}_{0.5})\text{O}_3$ nanofibers. At each temperature, a straight-line equation was fitted in both the investigated regions for the calculation of slopes (s). The calculated values of slopes (s) were plotted as a function of selected temperature for both the regions, as shown in Fig. 13c. We can observe that the values of slopes (s) in the region-I lie in the range from 1.0 to 1.1, which indicates an Ohmic type conduction [64] in the $\text{Pb}(\text{Zr}_{0.5}\text{Ti}_{0.5})\text{O}_3$ nanofibers. This is because, that still the injected charge carriers are not significant, and the thermal equilibrium of the charge carriers is not disrupted. We can clearly observe this region at all the selected temperatures from 308 to 408 K at low voltages. However, the values of slopes (s) in the second region, varies from 1.4 to 1.6 which illustrates the transformation of conduction mechanism from ohmic behavior to some field-assisted-barrier (FAB) conduction [65]. The observed variation from the low voltage ohmic-conduction to the high FAB conduction is resulting in an exponential-dependency of the generated current at the applied voltage. This mechanism is ascribed to the hopping of which are in the form of thermally generated carriers (holes and/or electrons) amongst the localized-states that are contained in the forbidden band of the non-crystalline materials [66].

3.6 Piezoelectric properties of nanogenerator based on $\text{Pb}(\text{Zr}_{0.5}\text{Ti}_{0.5})\text{O}_3$ nanofibers

Piezoelectric nanogenerators, has the ability to harvest energy from mechanical energy, are appealing for

numerous applications such as self-powered micro/nanodevices, smart wearable systems, implantable biosensors, wireless sensors, and nanorobotics [11, 67–69]. Piezoelectric nanofibers based nanogenerators have potential applications to power-up these devices via the transformation of mechanical energy into electrical energy [70]. Though, the piezoelectric voltage-constant of PZT nanomaterials is higher than the other piezoelectric materials reported for the nanogenerators in the literature [1, 28, 29].

Here we investigate a $\text{Pb}(\text{Zr}_{0.5}\text{Ti}_{0.5})\text{O}_3$ nanofibers based piezoelectric nanogenerator. The fabricated PZT nanofibers based nanogenerator was tested by Keithley 2182A nano-voltmeter for the generation of voltage. Simple fingers applied pressure was used as a dynamic periodic load on the top of the nanogenerator, during which the positive and negative voltage outputs were observed, as described in Fig. 14a, b. The positive voltage was generated due to the applied load whereas the negative voltage distribution was generated owing to the reverse flowing carriers after the removal of external load, and the piezo-potential disappeared. The maximum output voltage measured during the application of periodic stress to the nanogenerator was ~ 40 V. This output voltage is much enhanced from the reported output voltage of ~ 1.4 V by Chen et. al. [11]. The large-scale generated output voltage depends on the mechanical and electrical properties of the prepared piezoelectric materials, i.e., how much pressure can the materials accommodate to be applied on the surface to nanogenerator to produce voltage without any damage in their structure. These results suggest the excellent mechanical, flexible, and piezoelectric properties of the prepared

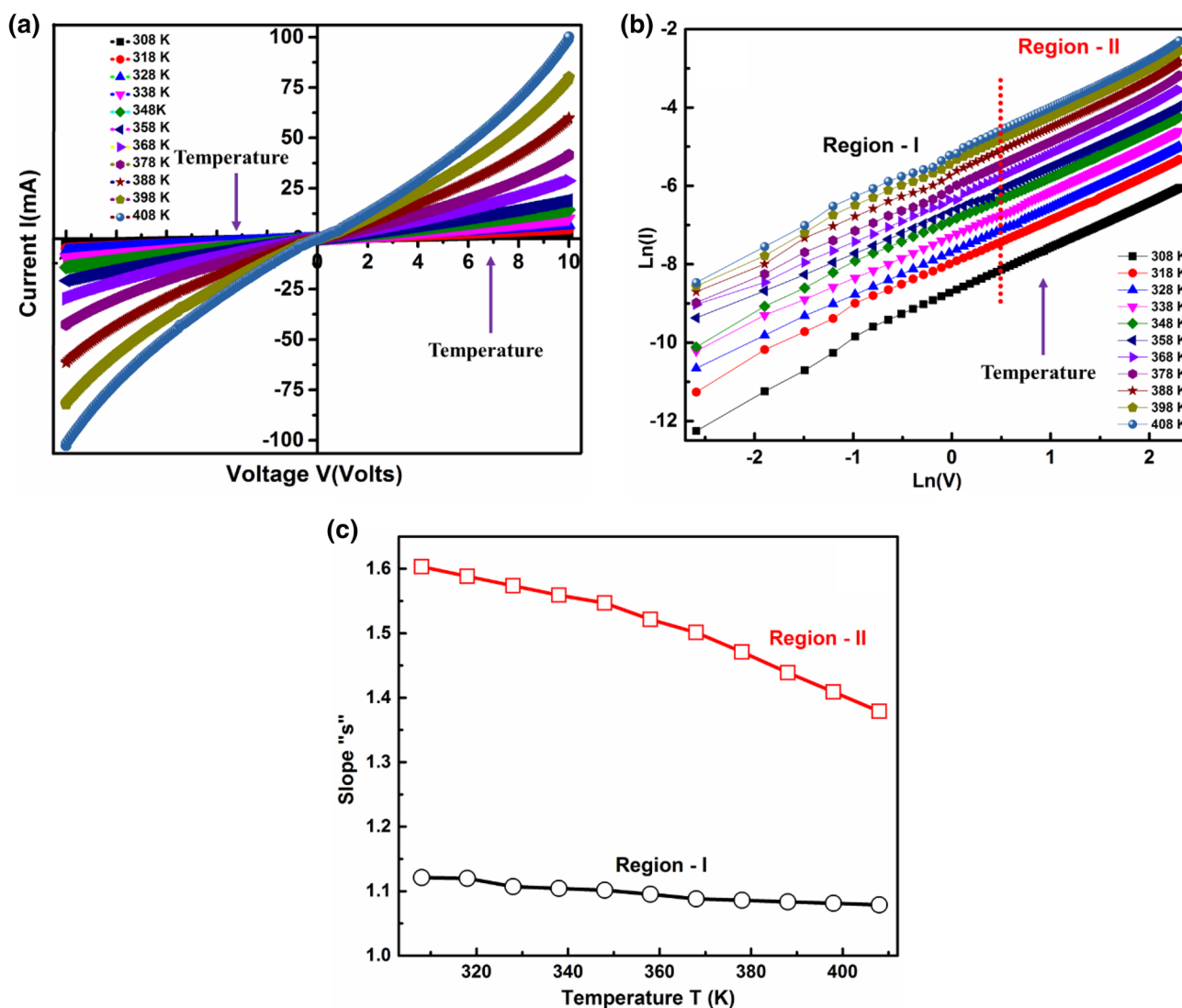


Fig. 13 **a** I - V curves of $\text{Pb}(\text{Zr}_{0.5}\text{Ti}_{0.5})\text{O}_3$ nanofibers calcined at 600°C , **b** I - V curves on \ln - \ln scale, and **c** variation of slopes (s) with temperature

$\text{Pb}(\text{Zr}_{0.5}\text{Ti}_{0.5})\text{O}_3$ nanofibers in the fabrication of nanogenerators for commercial applications.

4 Conclusion

PVP/PZT composite nanofibers were prepared using an electrospinning technique. The desired single-phase $\text{Pb}(\text{Zr}_{0.5}\text{Ti}_{0.5})\text{O}_3$ nanofibers of an average diameter ~ 96 nm with the uniform morphology but porous surface were obtained after the calcination of the composite nanofibers at 600°C for eight hours. Different PVP concentrations (10–30 wt%) were used for the optimization of PZT nanofibers. The results showed that PVP concentration played a significant

role in the fabrication, homogeneity, uniformity, porosity, and especially diameter variations of the PZT nanofibers while keeping other parameters constant. The TG/DTA analysis showed that the weight of the PVP/PZT composite nanofibers remained constant at temperatures $\geq 480^\circ\text{C}$, and the total weight loss throughout the employed heating cycle was $\sim 74\%$. The SEM images demonstrated that the diameter of the as-dried composite nanofibers was ~ 200 nm, with a smooth surface. The diameter of $\text{Pb}(\text{Zr}_{0.5}\text{Ti}_{0.5})\text{O}_3$ nanofibers decreased from ~ 200 to ~ 96 nm, and their surface became porous when calcined at 600°C . XRD and FTIR results demonstrated that at low temperatures, crystallinity did not exist in the nanofibers and when the sample was calcined at 600°C , single-phase perovskite $\text{Pb}(\text{Zr}_{0.5}\text{Ti}_{0.5})\text{O}_3$ nanofibers formed. The broad XRD peaks indicated that these

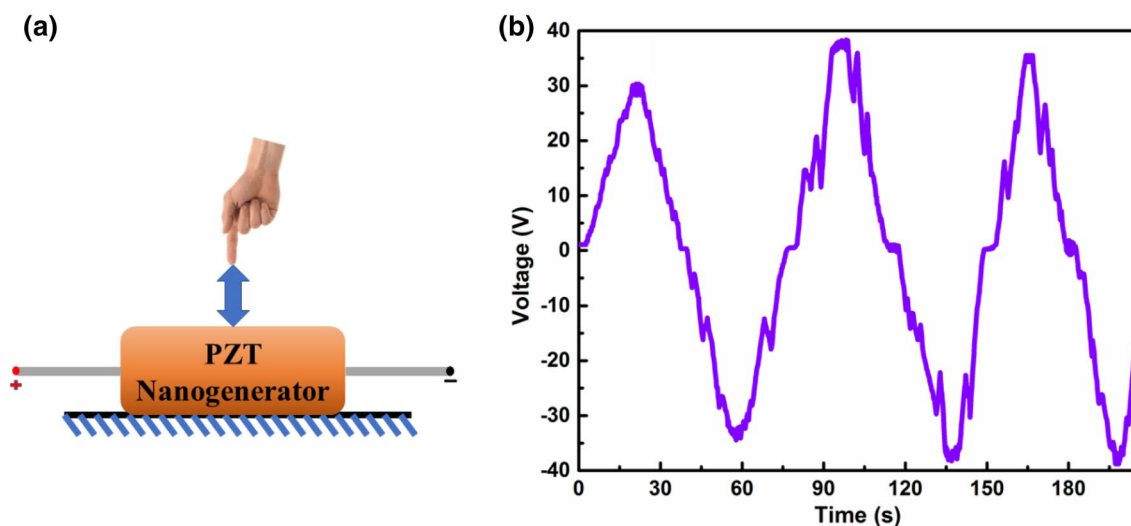


Fig. 14 **a** Schematic representation of a nanogenerator with simple finger applied the dynamic periodic load, and **b** Voltage output of PZT nanogenerator, recorded with the finger applied dynamic periodic load on the top surface of the nanogenerator

nanofibers comprised nano-crystallites. The crystal structure of the prepared PZT nanofibers was tetragonal with space group $P4mm$. EDS represented the chemical constituents of the calcined PZT nanofibers when calcined at $600\text{ }^{\circ}\text{C}$, and hence no impurity elements could be detected. The UV–Vis result suggested that PZT has a direct and wide bandgap, which is considered effective for significant piezoelectric effects in nanogenerators. The bandgap energy was calculated using the Tauc plot, and the estimated bandgap was $\sim 3.5\text{ eV}$ that is in reasonable agreement with the literature. Impedance spectroscopy findings demonstrated that the PZT nanofibers perform like a semiconductor material in the applied ranges of frequency and temperature. From the Impedance spectroscopy study, as the temperature decreases, the peaks shift from high frequencies to low frequencies, suggesting a reduction in the mobility of the charge-carriers in the PZT nanofibers. Additionally, with a decrease in temperature, the peaks broadening revealed the existence of more than one relaxation phenomenon occurring in the PZT nanofibers. The spectroscopic-plots were further evaluated and the related capacitance C_1 and C_2 were calculated, having values in the range of $(10^{-11}–10^{-12}\text{ F})$ and $(10^{-10}–10^{-11}\text{ F})$ respectively. These results suggested that two different electro-active regions (grain/bulk and grain-boundary) were present in the PZT nanofibers. From the dielectric results, it is evident that dielectric constant-decreases when the frequency increases as expected. The dielectric-constant of $\text{Pb}(\text{Zr}_{0.5}\text{Ti}_{0.5})\text{O}_3$ nanofibers recorded at room temperature and at a high frequency 2 MHz was ~ 1827 . This high value of the dielectric constant is considered important for piezoelectric performance. In the case of DC measurements, at selected temperatures ($308–408\text{ K}$), the observed non-linearity of $I–V$ characteristic curves indicated a semiconductor

behavior. Temperature-dependent $I–V$ electrical transport characteristics of the PZT nanofibers demonstrated the presence of two distinct regions and the dominant conduction mechanism was probably field-assisted-barrier conduction. Ohmic like behavior was observed at low-voltages, whereas field-assisted-barrier conduction was observed at high voltages. Based on $\text{Pb}(\text{Zr}_{0.5}\text{Ti}_{0.5})\text{O}_3$ nanofibers, an integrated nanogenerator was developed, which gave an ultra-high-output voltage of $\sim 40\text{ V}$. The investigated proto-type nanogenerator can be used as a cantilever for the periodic power generation.

Acknowledgements The authors acknowledge the financial support via the Indigenous 5000 Ph.D. fellowship program (Phase–II, Batch–III) in Science and Technology, and NRP-5198-(2016) by HEC, Pakistan. The authors also acknowledge the laboratory facilities provided by Materials Research Laboratory (MRL), Department of Physics, University of Peshawar, KP, Pakistan.

References

1. Z.L. Wang, J. Song, *Science* **312**(5771), 242–246 (2006). <https://doi.org/10.1126/science.1124005>
2. M. Ashraf, I. Khan, M. Usman, A. Khan, S.S. Shah, A.Z. Khan, K. Saeed, M. Yaseen, M.F. Ehsan, M.N. Tahir, N. Ullah, *Chem. Res. Toxicol.* **33**(6), 1292–1311 (2020). <https://doi.org/10.1021/acs.chemrestox.9b00308>
3. Z.L. Wang, G. Zhu, Y. Yang, S. Wang, C. Pan, *Mater. Today* **15**(12), 532–543 (2012). [https://doi.org/10.1016/S1369-7021\(13\)70011-7](https://doi.org/10.1016/S1369-7021(13)70011-7)
4. L. Gu, J. Liu, N. Cui, Q. Xu, T. Du, L. Zhang, Z. Wang, C. Long, Y. Qin, *Nat. Commun.* **11**(1), 1030 (2020). <https://doi.org/10.1038/s41467-020-14846-4>
5. K.-I. Park, S. Xu, Y. Liu, G.-T. Hwang, S.-J.L. Kang, Z.L. Wang, K.J. Lee, *Nano Lett.* **10**(12), 4939–4943 (2010). <https://doi.org/10.1021/nl102959k>

6. T. Karaki, K. Yan, M. Adachi, *Jpn. J. Appl. Phys.* **46**(10S), 7035 (2007). <https://doi.org/10.1143/Jjap.46.7035>
7. R. Pferner, G. Thurn, F. Aldinger, *Mater. Chem. Phys.* **61**(1), 24–30 (1999). [https://doi.org/10.1016/S0254-0584\(99\)00108-X](https://doi.org/10.1016/S0254-0584(99)00108-X)
8. G. Shirane, R. Newnham, R. Pepinsky, *Phys. Rev.* **96**(3), 581 (1954). <https://doi.org/10.1103/PhysRev.96.581>
9. R. Maeda, J. Tsauro, S. Lee, M. Ichiki, *J. Electroceram.* **12**(1–2), 89–100 (2004). <https://doi.org/10.1023/B:JECR.0000034003.47433.7e>
10. Y.-C. Hsu, C.-C. Wu, C.-C. Lee, G. Cao, I. Shen, *Sens. Actuators A* **116**(3), 369–377 (2004). <https://doi.org/10.1016/j.sna.2004.05.024>
11. X. Chen, S. Xu, N. Yao, Y. Shi, *Nano Lett.* **10**(6), 2133–2137 (2010). <https://doi.org/10.1021/nl100812k>
12. M. Sobocinski, M. Leinonen, J. Juuti, N. Mantyniemi, H. Jantunen, *Sens. Actuators A* **216**, 370–375 (2014). <https://doi.org/10.1016/j.sna.2014.06.017>
13. D. Damjanovic, *J. Am. Ceram. Soc.* **88**(10), 2663–2676 (2005). <https://doi.org/10.1111/j.1551-2916.2005.00671.x>
14. J. Chang, M. Dommer, C. Chang, L. Lin, *Nano Energy* **1**(3), 356–371 (2012). <https://doi.org/10.1016/j.nanoen.2012.02.003>
15. A. Warner, M. Onoe, G. Coquin, *J. Acoust. Soc. Am.* **42**(6), 1223–1231 (1967). <https://doi.org/10.1121/1.1910709>
16. L. Egerton, D.M. Dillon, *J. Am. Ceram. Soc.* **42**(9), 438–442 (1959). <https://doi.org/10.1111/j.1151-2916.1959.tb12971.x>
17. H. Kozuka, S. Takenaka, H. Tokita, M. Okubayashi, *J. Eur. Ceram. Soc.* **24**(6), 1585–1588 (2004). [https://doi.org/10.1016/S0955-2219\(03\)00402-3](https://doi.org/10.1016/S0955-2219(03)00402-3)
18. E.M. Alkoy, C. Dagdeviren, M. Papila, *J. Am. Ceram. Soc.* **92**(11), 2566–2570 (2009). <https://doi.org/10.1111/j.1551-2916.2009.03261.x>
19. M. Khajelakzay, E. Taheri-Nassaj, *Mater. Lett.* **75**, 61–64 (2012). <https://doi.org/10.1016/j.matlet.2012.01.082>
20. J.S. Yun, C.K. Park, J.H. Cho, J.-H. Paik, Y.H. Jeong, J.-H. Nam, K.-R. Hwang, *Mater. Lett.* **137**, 178–181 (2014). <https://doi.org/10.1016/j.matlet.2014.08.139>
21. L.-Q. Cheng, J.-F. Li, *J. Materiomics* **2**(1), 25–36 (2016). <https://doi.org/10.1016/j.jmat.2016.02.003>
22. X. Gao, J. Yang, J. Wu, X. Xin, Z. Li, X. Yuan, X. Shen, S. Dong, *Adv. Mater. Technol.* **5**(1), 1900716 (2020). <https://doi.org/10.1002/admt.201900716>
23. S.S. Shah, K. Hayat, S. Ali, K. Rasool, Y. Iqbal, *Mater. Sci. Semicond. Process.* **90**, 65–71 (2019). <https://doi.org/10.1016/j.mssp.2018.10.008>
24. K. Hayat, S.S. Shah, M. Yousaf, M.J. Iqbal, M. Ali, S. Ali, M. Ajmal, Y. Iqbal, *Mater. Sci. Semicond. Process.* **41**, 364–369 (2016). <https://doi.org/10.1016/j.mssp.2015.10.009>
25. Y. Xin, J. Zhu, H. Sun, Y. Xu, T. Liu, C. Qian, *Ferroelectrics* **526**(1), 140–151 (2018). <https://doi.org/10.1080/00150193.2018.1456304>
26. L. Gu, N. Cui, L. Cheng, Q. Xu, S. Bai, M. Yuan, W. Wu, J. Liu, Y. Zhao, F. Ma, Y. Qin, Z.L. Wang, *Nano Lett.* **13**(1), 91–94 (2013). <https://doi.org/10.1021/nl303539c>
27. H. Liu, J. Zhong, C. Lee, S.-W. Lee, L. Lin, *Appl. Phys. Rev.* **5**(4), 041306 (2018). <https://doi.org/10.1063/1.5074184>
28. R. Yang, Y. Qin, L. Dai, Z.L. Wang, *Nat. Nanotechnol.* **4**(1), 34–39 (2009). <https://doi.org/10.1038/nnano.2008.314>
29. R. Yang, Y. Qin, C. Li, G. Zhu, Z.L. Wang, *Nano Lett.* **9**(3), 1201–1205 (2009). <https://doi.org/10.1021/nl803904b>
30. J. Širc, R. Hobzová, N. Kostina, M. Munzarová, M. Juklíčková, M. Lhotka, Š. Kubinová, A. Zájčová, J. Michálek, *J. Nanomater.* **2012**, 121 (2012). <https://doi.org/10.1155/2012/327369>
31. Z.-M. Huang, Y.-Z. Zhang, M. Kotaki, S. Ramakrishna, *Compos. Sci. Technol.* **63**(15), 2223–2253 (2003). [https://doi.org/10.1016/S0266-3538\(03\)00178-7](https://doi.org/10.1016/S0266-3538(03)00178-7)
32. B. Tarus, N. Fadel, A. Al-Oufy, M. El-Messiry, *Alex. Eng. J.* **55**(3), 2975–2984 (2016). <https://doi.org/10.1016/j.aej.2016.04.025>
33. S.L. Shenoy, W.D. Bates, H.L. Frisch, G.E. Wnek, *Polymer* **46**(10), 3372–3384 (2005). <https://doi.org/10.1016/j.polymer.2005.03.011>
34. R. Festag, S.D. Alexandratos, D.C. Joy, B. Wunderlich, B. Annis, K.D. Cook, *J. Am. Soc. Mass Spectrom.* **9**(4), 299–304 (1998). [https://doi.org/10.1016/S1044-0305\(98\)00004-X](https://doi.org/10.1016/S1044-0305(98)00004-X)
35. D.-Y. Lee, J.-Y. Park, K.-H. Lee, J.-H. Kang, Y.-J. Oh, N.-I. Cho, *Curr. Appl. Phys.* **11**(5), 1139–1143 (2011). <https://doi.org/10.1016/j.cap.2011.02.011>
36. S. Yoshikawa, U. Selvaraj, P. Moses, J. Withams, R. Meyer, T. Shrout, *J. Intell. Mater. Syst. Struct.* **6**(2), 152–158 (1995). <https://doi.org/10.1177/1045389X9500600202>
37. S. Tungprapa, T. Puangparn, M. Weerasombut, I. Jangchud, P. Fakum, S. Semongkhon, C. Meechaisue, P. Supaphol, *Cellulose* **14**(6), 563–575 (2007). <https://doi.org/10.1007/s10570-007-9113-4>
38. K. Raju, P.V. Reddy, *Curr. Appl. Phys.* **10**(1), 31–35 (2010). <https://doi.org/10.1016/j.cap.2009.04.017>
39. C. Qizheng, D. Xiangting, W. Jinxian, L. Mei, *J. Rare Earths* **26**(5), 664–669 (2008). [https://doi.org/10.1016/S1002-0721\(08\)60158-1](https://doi.org/10.1016/S1002-0721(08)60158-1)
40. N. Dharmaraj, C. Kim, *H. Kim, Mater. Lett.* **59**(24), 3085–3089 (2005). <https://doi.org/10.1016/j.matlet.2005.05.040>
41. A.M. Smith, S. Nie, *Acc. Chem. Res.* **43**(2), 190–200 (2010). <https://doi.org/10.1021/ar9001069>
42. S. Ahn, S. Jung, J. Gwak, A. Cho, K. Shin, K. Yoon, D. Park, H. Cheong, J.H. Yun, *Appl. Phys. Lett.* **97**(2), 021905 (2010). <https://doi.org/10.1063/1.3457172>
43. Z. Lu, M. Hanna, A. Majerfeld, *Appl. Phys. Lett.* **64**(1), 88–90 (1994). <https://doi.org/10.1063/1.110877>
44. I.A. Buliyaminu, M.A. Aziz, S.S. Shah, A.K. Mohamedkhaier, Z.H. Yamani, *Arab. J. Chem.* **13**(3), 4785–4796 (2020). <https://doi.org/10.1016/j.arabjc.2019.12.013>
45. M.S. Hybertsen, S.G. Louie, *Phys. Rev. Lett.* **55**(13), 1418 (1985). <https://doi.org/10.1103/PhysRevLett.55.1418>
46. H. Lee, Y.S. Kang, S.-J. Cho, B. Xiao, H. Morkoç, T.D. Kang, G.S. Lee, J. Li, S.-H. Wei, P. Snyder, *J. Appl. Phys.* **98**(9), 094108 (2005). <https://doi.org/10.1063/1.2128043>
47. I. Boerasu, L. Pintilie, M. Pereira, M. Vasilevskiy, M. Gomes, *J. Appl. Phys.* **93**(8), 4776–4783 (2003). <https://doi.org/10.1063/1.1562009>
48. S. Pandey, A. James, R. Raman, S. Chatterjee, A. Goyal, C. Prakash, T. Goel, *Phys. B* **369**(1), 135–142 (2005). <https://doi.org/10.1016/j.physb.2005.08.024>
49. M.K. Gupta, J. Aneesh, R. Yadav, K. Adarsh, S.-W. Kim, *J. Appl. Phys.* **121**(17), 175103 (2017). <https://doi.org/10.1063/1.4982668>
50. M.S. Al-Ruqeishi, T. Mohiuddin, B. Al-Habsi, F. Al-Ruqeishi, A. Al-Fahdi, A. Al-Khusaibi, *Arab. J. Chem.* **12**(8), 5173–5179 (2019). <https://doi.org/10.1016/j.arabjc.2016.12.010>
51. J. Tian, C. Lai, G. Feng, D. Banerjee, W. Li, N.C. Kar, *Int. J. Sustain. Energy* **39**(1), 88–100 (2020). <https://doi.org/10.1080/14786451.2019.1657866>
52. J. Nelson, Y. Hu, *J. Phys. D* **38**(2), 213 (2005). <https://doi.org/10.1088/0022-3727/38/2/005>
53. M. Idrees, M. Nadeem, M. Hassan, *J. Phys. D* **43**(15), 155401 (2010). <https://doi.org/10.1088/0022-3727/43/15/155401>
54. N.C.D. Nath, S.S. Shah, M.A.A. Qasem, M.H. Zahir, M.A. Aziz, *ChemistrySelect* **4**(31), 9079–9083 (2019). <https://doi.org/10.1002/slct.201900891>
55. D.C. Sinclair, A.R. West, *J. Appl. Phys.* **66**(8), 3850–3856 (1989). <https://doi.org/10.1063/1.344049>
56. J.T. Irvine, D.C. Sinclair, A.R. West, *Adv. Mater.* **2**(3), 132–138 (1990). <https://doi.org/10.1002/adma.19900020304>

57. A. Kumar, N.M. Murari, R.S. Katiyar, J. Alloys Compd. **469**(1), 433–440 (2009). <https://doi.org/10.1016/j.jallcom.2008.01.130>
58. R. Kambale, P. Shaikh, C. Bhosale, K. Rajpure, Y. Kolekar, Smart Mater. Struct. **18**(8), 085014 (2009). <https://doi.org/10.1088/0964-1726/18/8/085014>
59. Y. Hosono, Y. Yamashita, IEEE Trans. Ultrason. Ferroelectr. Freq. Control **52**(10), 1823–1828 (2005). <https://doi.org/10.1109/tuffc.2005.1561638>
60. B. Jaffe, R. Roth, S. Marzullo, J. Appl. Phys. **25**(6), 809–810 (1954). <https://doi.org/10.1063/1.1721741>
61. J. Ryu, A.V. Carazo, K. Uchino, H.-E. Kim, J. Electroceram. **7**(1), 17–24 (2001). <https://doi.org/10.1023/A:1012210609895>
62. M.J. Schulz, M.J. Sundaresan, J. Mcmichael, D. Clayton, R. Sadler, B.J.J.O.I.M.S. Nagel, J. Intell. Mater. Syst. Struct. **14**(11), 693–705 (2003). <https://doi.org/10.1177/10453889x03038577>
63. A. Campbell, D. Bradley, D. Lidzey, J. Appl. Phys. **82**(12), 6326–6342 (1997). <https://doi.org/10.1063/1.366523>
64. A. Kaiser, Y. Park, Synth. Met. **152**(1–3), 181–184 (2005). <https://doi.org/10.1016/j.synthmet.2005.07.245>
65. J. Yeargan, H. Taylor, J. Appl. Phys. **39**(12), 5600–5604 (1968). <https://doi.org/10.1063/1.1656022>
66. M. Nadeem, A. Javed, M. Wasif, Braz. J. Phys. **39**(2), 280–282 (2009). <https://doi.org/10.1590/S0103-97332009000300006>
67. Y. Gao, Z.L. Wang, Nano Lett. **7**(8), 2499–2505 (2007). <https://doi.org/10.1021/nl071310j>
68. G. Zhu, R. Yang, S. Wang, Z.L. Wang, Nano Lett. **10**(8), 3151–3155 (2010). <https://doi.org/10.1021/nl101973h>
69. W. Wu, S. Bai, M. Yuan, Y. Qin, Z.L. Wang, T. Jing, ACS Nano **6**(7), 6231–6235 (2012). <https://doi.org/10.1021/nm3016585>
70. S. Xu, Z.L. Wang, Nano Res. **4**(11), 1013–1098 (2011). <https://doi.org/10.1007/s12274-011-0160-7>

Publisher's Note Springer Nature remains neutral with regard to jurisdictional claims in published maps and institutional affiliations.